



OPEN

Performance simulation of the perovskite solar cells with Ti_3C_2 MXene in the SnO_2 electron transport layer

Mahdiyeh Meskini[✉] & Saeid Asgharizadeh

MXenes, a class of two-dimensional (2D) transition metal carbides and nitrides, have a wide range of potential applications due to their unique electronic, optical, plasmonic, and other properties. SnO_2 – Ti_3C_2 MXene with different contents of Ti_3C_2 (0.5, 1.0, 2.0, 2.5 wt%), experimentally, has been used as electron transport layers (ETLs) in Perovskite Solar Cells (PSCs). The SCAPS-1D simulation software could simulate a perovskite solar cell comprised of $\text{CH}_3\text{NH}_3\text{PbI}_3$ absorber and SnO_2 (or SnO_2 – Ti_3C_2) ETL. The simulation results like Power Conversion Efficiency (PCE), Open circuit voltage (V_{oc}), Short circuit current density (J_{sc}), Fill Factor (FF), and External Quantum Efficiency (EQE) have been compared within samples with different weight percentages of Ti_3C_2 MXene incorporated in ETL. Reportedly, the ETL of SnO_2 with Ti_3C_2 (1.0 wt%) effectively increases PCE from 17.32 to 18.32%. We simulate the role of MXene in changing the ideality factor (n_{id}), photocurrent (J_{ph}), built-in potential (V_{bi}), and recombination resistance (R_{rec}). The study of interface recombination currents and electric field shows that cells with 1.0 wt% of MXene in SnO_2 ETL have higher values of ideality factor, built-in potential, and recombination resistance. The correlation between these values and cell performance allows one to conclude the best cell performance for the sample with 1.0 wt% of MXene in SnO_2 ETL. With an optimization procedure for this cell, an efficiency of 27.81% is reachable.

Keywords Perovskite solar cell, Ti_3C_2 MXene, SCAPS-1D, Electron transport layer, Photocurrent, Built-in potential, Ideality factor

Methylammonium lead iodide ($\text{CH}_3\text{NH}_3\text{PbI}_3$) was used in solar cells for the first time in 2009 by Miyaska et al.¹. Metal halide perovskites have unique properties that justify their use in solar cells^{2,3}. Technological progress in the field of organic–inorganic solar cells since the last decade has revolutionized the research field to achieve a better alternative to conventional energy sources. That is why the circle of research has been expanded mainly to these energy sources due to the better results. Many efforts have already been made leading to achieving higher power conversion efficiency (PCE) with much cheaper fabrication cost⁴. Perovskite solar cells (PSCs) have risen to stardom owing to their peculiar characteristics such as high charge carrier mobility, long free carrier diffusion length, broad and strong optical absorption, low exciton binding energy, as well as their cost-effective and easy solution process manufacture^{5,6}. Hybrid perovskites have great potential as being efficient, low-cost, and flexible materials for photovoltaic technology. Recent advancements have resulted in improved device stability and overall efficiency⁷. Metal halide perovskites are denoted by ABX_3 , where A refers to an organic cation, B to a metal cation, and X to a halogen anion⁸. PSC consists of an electron transport layer (ETL) as an electron collector and a hole transport layer (HTL) that effectively extracts holes from the perovskite absorber layer⁹. In PSCs, cell performance can be optimized by finding the best combination of ETL and HTL⁴. The effect of suitable HTLs is also significant as they influence the extraction and contribution to the instantaneous flow of light-generated holes from the perovskite absorber layer to the PSC cathode. The use of highly pure Spiro-OMeTAD HTL has been widely accepted in manufacturing and stability factors. At the same time, the selection of ETL is also necessary to reduce the recombination rate as well as to optimize the efficiency of PSC¹⁰. There must be a much better alignment in the energy bands between the HTL and the absorber layer to allow the transport of holes from the perovskite absorber layer to the HTL. The built-in (V_{bi}) electric field created due to the choice of contact metals in the back and front contacts helps to maintain an electric field throughout the device configuration, which enables smooth transport of charge carriers throughout the device⁹. Researchers have been working to improve

Faculty of Physics, University of Tabriz, Tabriz, Iran. ✉email: meskiniim@gmail.com

PSC performance for decades. However, the proper selection of materials related to the optimal thickness in the device structure is a much-needed approach to increase device efficiency¹¹. SnO₂ has emerged as a promising ETL in PSCs due to its optical transparency and environmental stability^{12–15}. In addition, the combination of SnO₂ with n-type semiconductors or highly conductive materials is an effective method for further enhancing the electrical conductivity of the ETLs^{16–18}. This improvement has led to an increase in the PCE of the solar cells^{19–21}. Recently, two-dimensional (2D) materials have been gaining significant attention as potential candidates for use in photovoltaic PSCs due to their unique optical and electronic properties^{22–24}. A new family of 2D materials, known as MXenes, has emerged. These materials are composed of transition metal carbides, nitrides, and carbonitrides, with a general formula of M_{n+1}X_nT_x (where n can be 1, 2, or 3). In this formula, M represents a transition metal like titanium or vanadium, while X stands for carbon or nitrogen. T_x refers to the surface-terminating functional groups. These materials have found significant applications in PSCs^{25–27}. The first studies on MXene's applications in PSCs date back to 2018, when they were used in absorber layers and ETLs^{28,29}. MXenes have been applied in the structure of PSCs to enhance their (PCE)³⁰. Surface termination in these materials can affect the density of states (DOS) and work function (WF)^{31,32}, offering new opportunities for PSC applications. Among the MXenes, Ti₃C₂ is an excellent additive for the SnO₂ ETL, which is commonly used in PSCs³³. Films of SnO₂ with different Ti₃C₂ contents (0.0, 0.5, 1.0, 2.0, 2.5 wt%) were prepared by spin-coating onto indium tin oxide (ITO) substrates³⁴. Photovoltaic devices were constructed using an architecture consisting of ITO/ETL/CH₃NH₃PbI₃/Spiro-OMeTAD/Ag.

It has been reported that incorporating MXenes into the ETL can decrease interface recombination, leading to higher PCEs for PSCs³⁵. It is useful to estimate the dominant recombination pathway to demonstrate the role of MXenes in influencing interfacial recombination. The ideality factor (n_{id}) is a parameter used to determine the dominant recombination mechanism in a semiconductor device²⁸. One common method to calculate the n_{id} is by measuring the open-circuit voltage (V_{OC}) of the light intensity³⁶. A n_{id} value of 1 indicates that the dominant recombination mechanism at play is the interface Shockley–Read–Hall (SRH) recombination³⁷. On the other hand, a n_{id} value close to 2 suggests that the absorber layer's dominant recombination mechanism is trap-assisted recombination^{38,39}. The n_{ids} between unity and two will predict interfacial and bulk recombination superposition.

Impedance spectroscopy (IS) is a versatile technique used to monitor electrical and electrochemical processes and profile the electronic structure in devices. During an IS measurement, a small-signal, sinusoidal electrical stimulus is applied to a sample, and its response is monitored at different frequencies⁴⁰. This technique is used to measure the resistive and capacitive behavior of an electrochemical system. This is done by applying an alternating current (AC) potential to the system at different frequencies and then measuring the alternating current response through the cell⁴¹. IS technique includes plotting the so-called Nyquist graph that illustrates the imaginary part of the complex impedance versus the real part of it. Fitting this graph, one could use the charge recombination resistance (R_{rec}) in the equivalent circuit⁴². In this study, we used IS to examine charge dynamics in the absorber layer and interfaces in simulated solar cells. This study aimed to investigate the changes in the IS response of PSCs and to identify the mechanisms responsible for the decrease in cell efficiency. Also, we calculated series resistance (R_s) in the equivalent circuit⁴³. We used simulation software called SCAPS-1D⁴⁴ to investigate how adding different weight percentages of Ti₃C₂ MXene to the SnO₂ ETL layer in a PSC structure (ITO/SnO₂ (ETL)/CH₃NH₃PbI₃/Spiro-OMeTAD/Ag) affected the photocurrent density (J_{ph}), n_{id} , and R_{rec} . The software considers the production and recombination of charge carriers in the layers and interfaces. Additionally, we studied the performance of PSCs with 1.0 wt.% MXene-assisted ETL for various thicknesses of the absorber and charge transport layers to optimize the structure and achieve the highest possible PCE.

Methodology and simulations

SCAPS-1D is a software used for one-dimensional simulations. It calculates energy bands, current–voltage characteristics, and external quantum efficiency by solving continuity equations for electrons and holes and the Poisson equation⁴⁵. The software can also calculate recombination profiles and electric field distribution for layers and interlayers. The basic continuity equations used by this software for electrons and holes are:

$$J_n = qn\mu_n E + qD_n \frac{\partial n}{\partial x}, \quad (1)$$

$$J_p = qp\mu_p E - qD_p \frac{\partial p}{\partial x}, \quad (2)$$

where μ_n and μ_p are the electron and hole mobility respectively, D_n (D_p) is the electron (hole) diffusion coefficient, E is the electric field, q is the electron charge, and p (n) is the hole (electron) density. The recombination rate of electrons and holes ($U_{n,p}$) can be calculated through the equations mentioned above:

$$\frac{\partial J_n}{\partial x} + G - U_n(n, p) = 0, \quad (3)$$

$$-\frac{\partial J_p}{\partial x} + G - U_p(n, p) = 0, \quad (4)$$

where G is the electron–hole generation rate.

In a recent experiment, researchers incorporated Ti₃C₂ MXene in SnO₂ ETL to enhance the efficiency of PSCs. To understand how this enhancement is achieved, simulations were conducted on two types of PSCs. The first one had the architecture of ITO/SnO₂/CH₃NH₃PbI₃/Spiro-OMeTAD/Ag, while the second one had the architecture

of ITO/SnO₂-Ti₃C₂ (0.5, 1.0, 2.0 and 2.5 wt.%) /CH₃NH₃PbI₃/Spiro-OMeTAD/Ag (Fig. 1). The simulation work used data provided by the original experimental work⁴⁴.

The material parameters for the pristine sample are selected from published experimental data and listed in Table 1. Interfacial parameters for simulation are shown in Table 2. In this table, N_A and N_D denote acceptor and donor densities, ε is relative permittivity, χ is electron affinity, E_g is band gap energy, and N_t is defect density. N_C and N_V are the effective densities of conduction and valance band states, respectively. To estimate the thickness of the layers, the SEM image provided in the experimental work³⁴ was used. In addition, the electron/hole thermal velocity for each layer was set to 10⁷ cm/s, simulated light conditions were AM1.5G, and the simulation temperature was 300 K. According to a study²⁸, incorporating Ti₃C₂ MXene into the layers of PSC does not affect the band gap energy. However, it does reduce the WF in the layers, which changes the electron affinity of the layers²⁸. This means that the band gap energy will remain the same for MXene-added structures. Moreover,

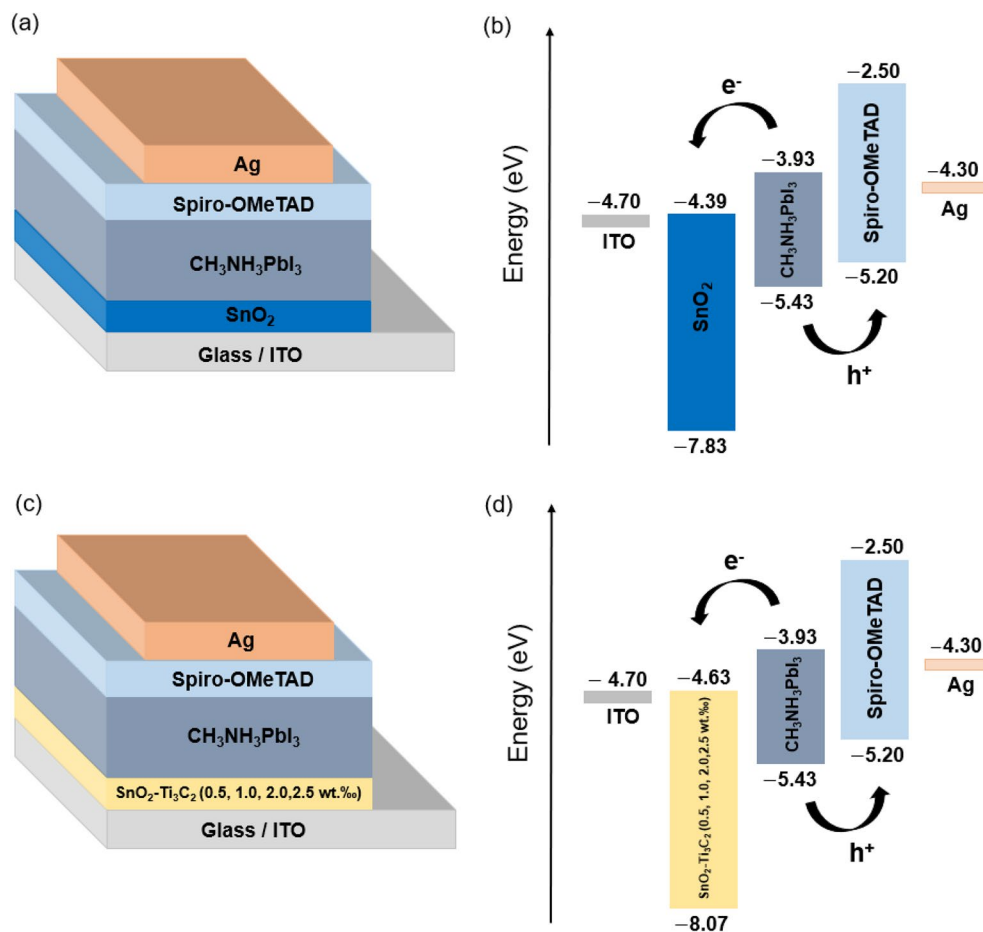


Figure 1. (a) Device architecture of ITO/SnO₂/CH₃NH₃PbI₃/Spiro-OMeTAD/Ag, and (b) its schematic energy level diagram. (c) Device architecture of ITO/SnO₂-Ti₃C₂/CH₃NH₃PbI₃/Spiro-OMeTAD/Ag, and (d) its schematic energy level diagram.

Parameter	ITO	SnO ₂ (ETL)	CH ₃ NH ₃ PbI ₃ (absorber)	Spiro-OMeTAD (HTL)
Thickness (nm)/ε	150 ^a /8.9 ^b	30 ^a /9.0 ^b	430 ^a /10.0 ^e	140 ^a /3.0 ^f
E _g /χ (eV)	3.5 ^c /4.5 ^c	3.44 ^a /4.39 ^a	1.5 ^a /3.93 ^a	2.7 ^a /2.5 ^a
N _C /N _V (×10 ¹⁹) (cm ⁻³)	0.22 ^c /1.8 ^c	0.22 ^b /1.8 ^b	0.1 ^e /0.1 ^e	10.0 ^f /10.0 ^f
N _D /N _A (×10 ¹⁹) (cm ⁻³)	100/-	1.0/-	-/4.0	-/7.0
N _t (×10 ¹⁵) (cm ⁻³)	1.0	1.0	0.001	0.1
μ _n /μ _p (cm ² /V s)	10.0 ^b /10.0 ^b	7.56 × 10 ⁻⁶ ^a /0.1 ^d	2.0 ^f /2.0 ^f	2.0 ^f /0.01 ^f
α (cm ⁻¹)	From spectrum ⁱ			

Table 1. Parameters used in the simulation by SCAPS for ITO/SnO₂/CH₃NH₃PbI₃/Spiro-OMeTAD/Ag PSCs structures. ^aRef. ³⁴, ^bRef. ⁴⁶, ^cRef. ⁴⁷, ^dRef. ⁴⁸, ^eRef. ⁴⁹, ^fRef. ⁵⁰, ⁱRef. ^{51,52}.

Parameter	ITO/ETL	ETL/Absorber	Absorber/HTL
Defect type	Neutral	Neutral	Neutral
Capture cross section electron (cm ²)	1.0×10^{-19}	1.0×10^{-19}	1.0×10^{-19}
Capture cross section hole (cm ²)	1.0×10^{-19}	1.0×10^{-19}	1.0×10^{-19}
Energetic distribution	Single	Single	Single
Reference for defect energy level E _i	Above the highest E _v	Above the highest E _v	Above the highest E _v
Energy with respect to reference (eV)	0.6	0.6	0.6
Total density (cm ⁻²)	1.0×10^{12}	1.0×10^9	1.0×10^9

Table 2. Interfacial parameters used in the simulation by SCAPS for ITO/SnO₂/CH₃NH₃PbI₃/Spiro-OMeTAD/Ag PSCs structures.

the electron affinity of the MXene-added ETL has been measured to be 4.63 eV³⁴. It has been reported that the efficiency enhancement of PSCs is mainly due to the increased mobility of the layers when MXene is added. In this work, we have adopted an electron mobility of 1.23×10^{-5} cm²/V s for the MXene-assisted ETL³⁴. This value shows an order of magnitude increase compared to the bare SnO₂ ETL. In the simulations, all parameters except for the MXene concentration in the ETL of the cells are kept constant. The values of carrier capture cross-section layers in PSCs with SnO₂ ETL and MXene-added ETL are considered to be 1×10^{-15} cm².

Results and discussion

The Fig. 2 illustrates the agreement between the experimental current density–Voltage (J–V) data for PSCs with SnO₂ and SnO₂-MXene (1.0 wt%) ETLs and simulation results. In the same figure, the theoretical External Quantum Efficiency (EQE) curve closely matches the measured one. This indicates that the model was able to successfully explain the process of photovoltaics. It's worth noting that the simulated photovoltaic parameters closely follow the measured values, as shown in the graph's inset.

The original paper³⁴ does not provide EQE data for the PSCs of SnO₂-MXene at varying concentrations (0.5, 1.5, 2.0, and 2.5 wt%). We present simulated J–V curves for the samples, which closely match the experimental ones shown in Fig. 3. In this figure, the calculated photovoltaic characteristics obtained from the fitting are being compared with the measured ones, where a high degree of concurrency can be seen between them. The generated EQE curves are shown in the insets.

For determining integrated current density, we combine the photon flow at a certain wavelength, leading to the flow of electrons leaving the solar cell at this wavelength⁵³. We have,

$$J_{SC,EQE} = -q \int_{\lambda_0}^{\lambda_{max}} EQE(\lambda) \Phi_{ph,\lambda} d\lambda, \quad (5)$$

where $\Phi_{ph,\lambda}$ is the photon flux of AM1.5. The simulated and experimental EQE spectra and their corresponding integrated currents density are depicted in Fig. 4. The calculated integrated current density for the SnO₂-based cell is 19.93 mA cm⁻². When 1.0 wt% MXene is added to the device, it increases to 20.29 mA cm⁻². The deviation between the integrated current from EQE and the values obtained from the simulation of J_{SC} values (presented in

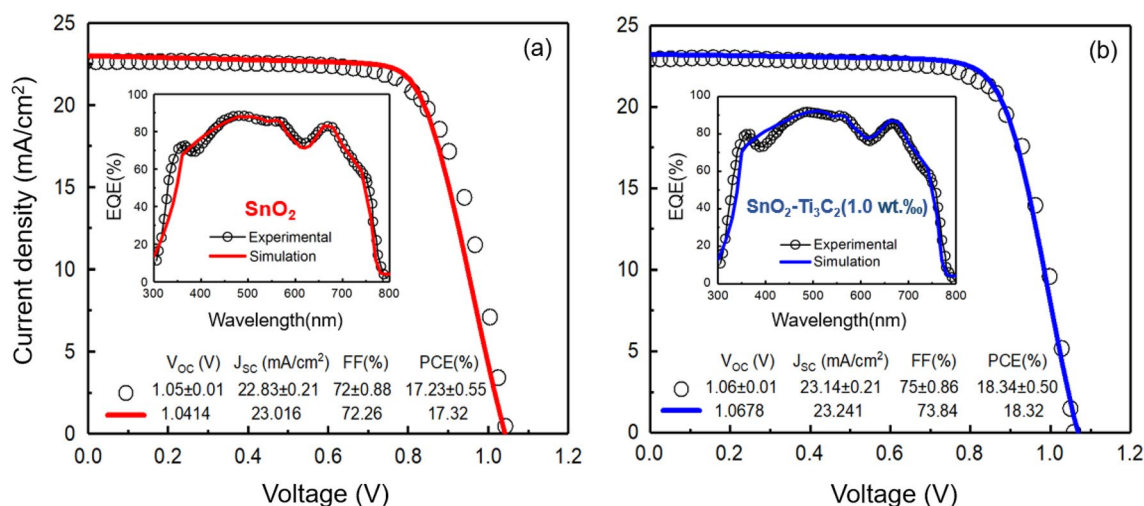


Figure 2. Simulated (solid line) and experimental (dotted) data of J–V and EQE curves of solar cells with different electron transport layers. (a) SnO₂, (b) SnO₂-Ti₃C₂ (1.0 wt%).

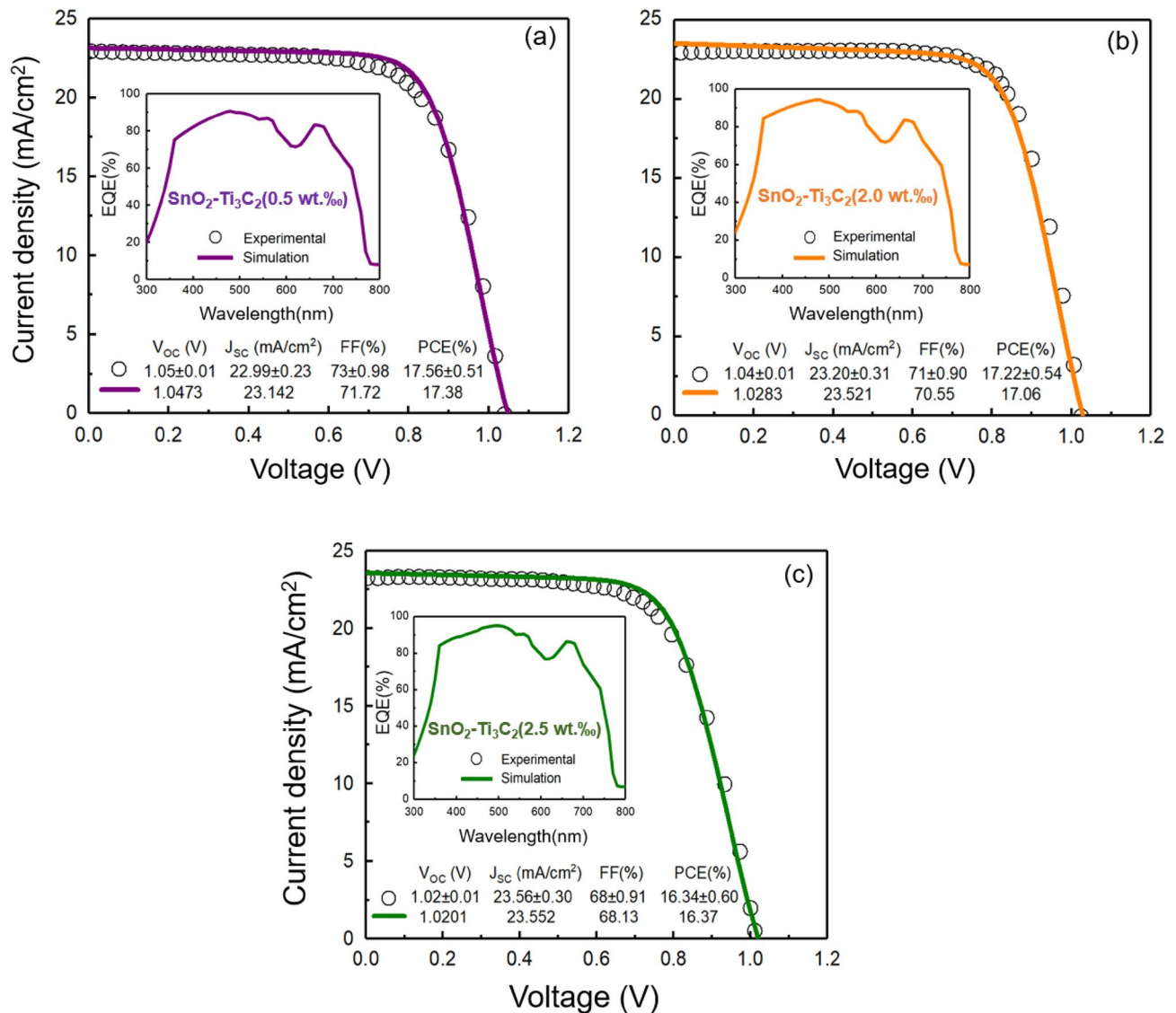


Figure 3. Simulated (solid line) and experimental (dotted) data of J–V and EQE curves of solar cells with different electron transport layers. (a) SnO₂-Ti₃C₂ (0.5 wt%), (b) SnO₂-Ti₃C₂ (2.0 wt%), and (c) SnO₂-Ti₃C₂ (2.5 wt%).

Fig. 2) is around 10%. This indicates good accuracy of our J–V measured values. The integrated current density of SnO₂-Ti₃C₂ (0.5 wt%), SnO₂-Ti₃C₂ (2.0 wt%), and SnO₂-Ti₃C₂ (2.5 wt%) are 20.13 mA cm⁻², 20.41 mA cm⁻², and 20.58 mA cm⁻², respectively. Figure 5 shows the result of the simulation of EQE and integrated current density for SnO₂-Ti₃C₂ (0.5 wt%), SnO₂-Ti₃C₂ (2.0 wt%), and SnO₂-Ti₃C₂ (2.5 wt%). It can be seen that the amount integrated current density follows the order of MXene weight percentage in the SnO₂ ETL.

The Nyquist plots of solar cells of different ETLs with recorded IS spectra are shown in Fig. 6. The R_{rec} s calculated from fitting the semicircle Nyquist plots are shown in the same Fig. The semicircle is observed for all conditions, and it starts at a high frequency and ends at a low frequency. This semicircle can be fitted to an equivalent circuit. The wires and ITO substrate are largely associated with R_s . The main observed semicircle represents R_{rec} , and the interfacial capacitance (C) at the ETL/perovskite interface³⁴. R_s is in series with other components and results in a shift in the Nyquist spectrum along the real axis away from the origin. The term R_{rec} denotes the phenomenon of electron capture, where an electron or hole moves from the conduction or valence band to a defect in the bandgap or to surface states^{54,55}. Capacitance in IS corresponds to the storage of electrical energy. Physically, capacitance arises either due material polarisation (geometric capacitance), or due to local inhomogeneity in the distribution of free charge (electrochemical capacitance), usually related to charge dynamics. R_{rec} is inversely proportional to charge recombination. Higher R_{rec} suggests lower carrier recombination (better hole-blocking ability)³⁴. In Fig. 6, Nyquist plots are drawn for voltages of 0 V, 0.4 V and V_{oc}. Among the PSCs of ETL with MXene, the resistance value of R_{rec} is ordered as SnO₂-Ti₃C₂ (1.0 wt%) > SnO₂-Ti₃C₂ (0.5 wt%) > SnO₂-Ti₃C₂ (2.0 wt%) > SnO₂-Ti₃C₂ (2.5 wt%), where a higher resistance is better for electron collection. This implies that the least charge recombination occurs at the interface, resulting in the highest FF of SnO₂-Ti₃C₂ (1.0 wt%). This

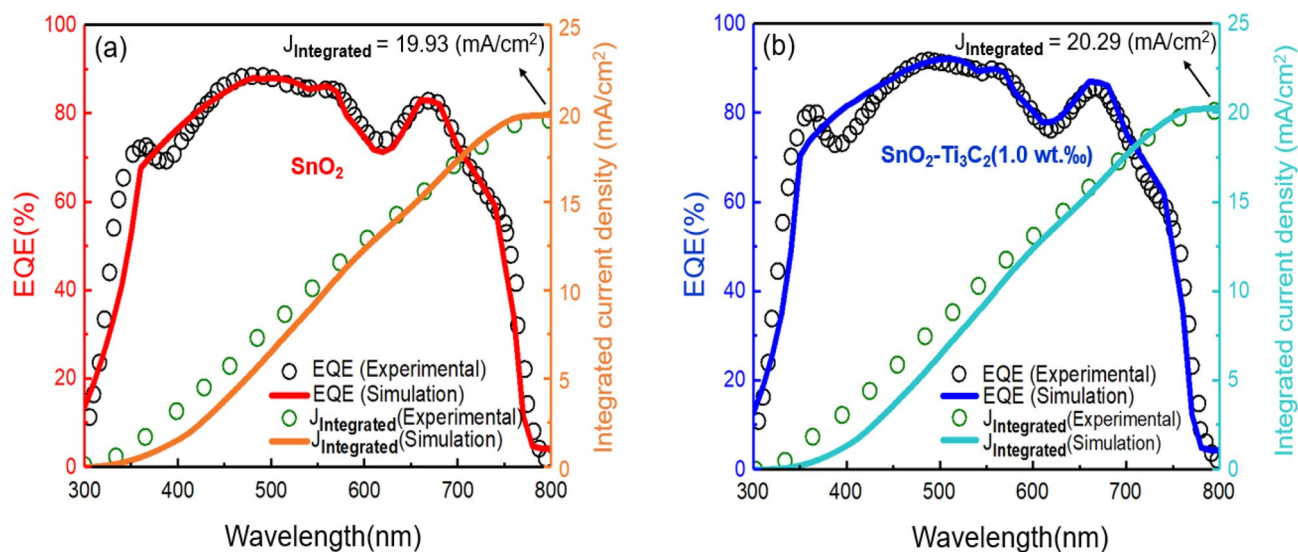


Figure 4. Simulated (solid line) and experimental (dotted) data of EQE spectra and the corresponding integrated current densities for the PSCs. (a) SnO₂, (b) SnO₂-Ti₃C₂ (1.0 wt.%).

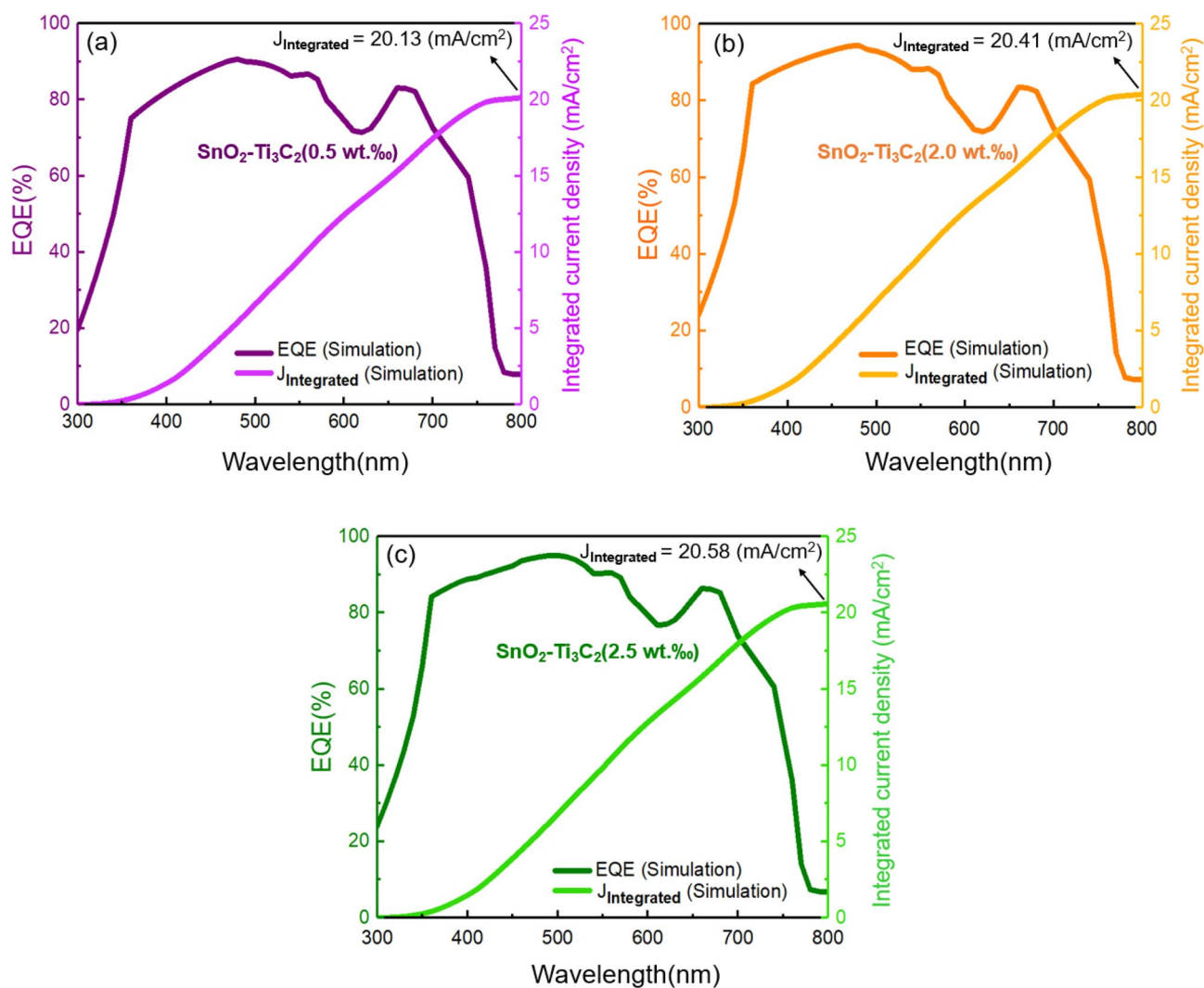


Figure 5. Simulated (solid line) data of EQE spectra and the corresponding integrated current densities for the PSCs. (a) SnO₂-Ti₃C₂ (0.5 wt.%), (b) SnO₂-Ti₃C₂ (2.0 wt.%), and (c) SnO₂-Ti₃C₂ (2.5 wt.%).

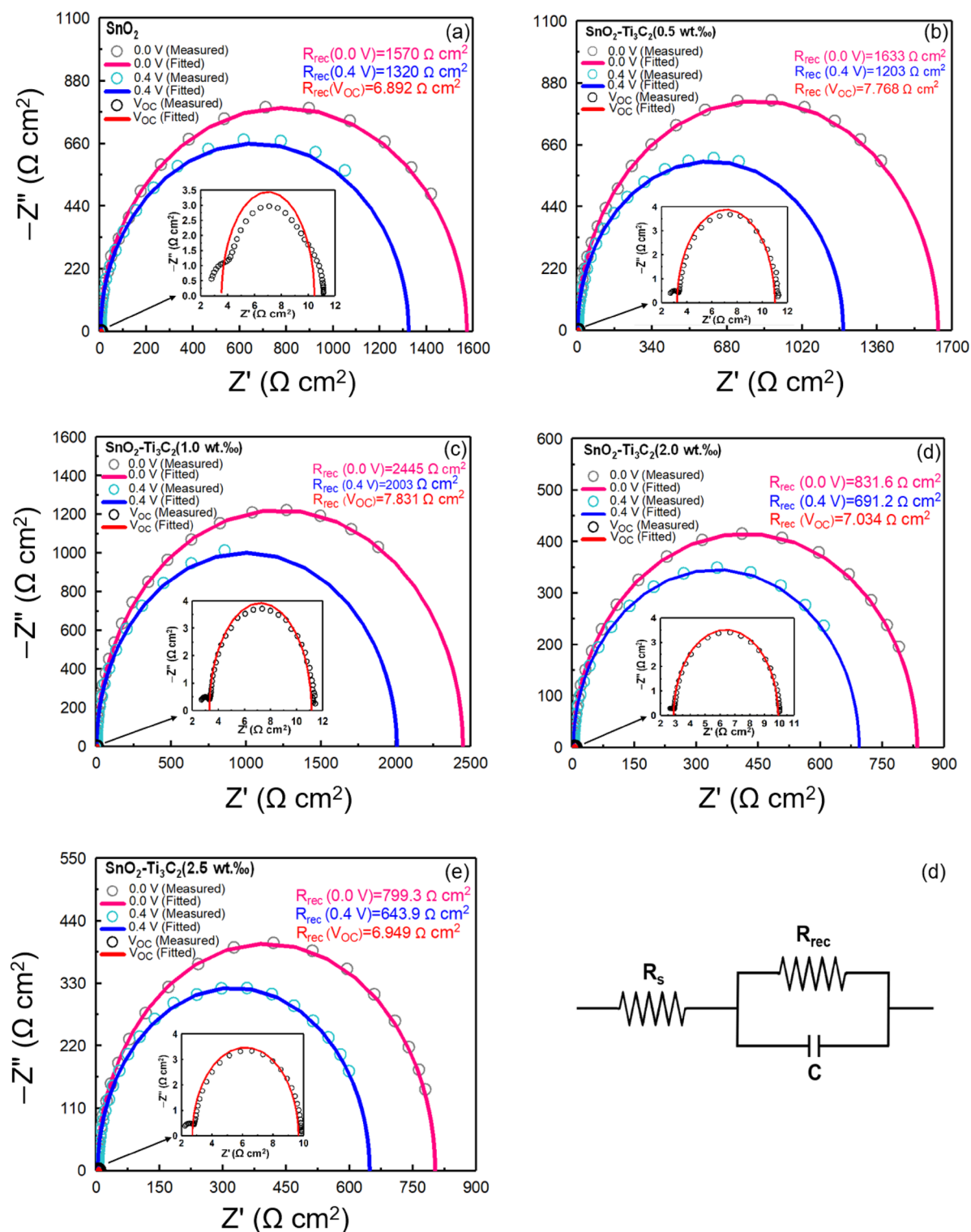


Figure 6. Measured (dotted) and fitted (solid line) data of Nyquist plots of PSCs fabricated with the different ETLs. (a) SnO_2 , (b) $\text{SnO}_2\text{-Ti}_3\text{C}_2$ (0.5 wt%), (c) $\text{SnO}_2\text{-Ti}_3\text{C}_2$ (1.0 wt%), (d) $\text{SnO}_2\text{-Ti}_3\text{C}_2$ (2.0 wt%), (e) $\text{SnO}_2\text{-Ti}_3\text{C}_2$ (1.0 wt%), and (f) Circuit representation of a fundamental relaxation process with characteristic resistance and capacitance.

can be partly attributed to the better electron extraction due to the addition of Ti_3C_2 . The performance improvement can practically be explained by R_{rec} . In general, higher R_{rec} corresponds to higher PCE.

Figure 7a displays the variation of V_{OC} values with illumination for cells with and without MXene. It is evident that the V_{OC} increases with the intensity of illumination; however, it almost reaches saturation at high light intensity. We used^{56,57} to calculate the n_{id} s.

$$n_{id} = \frac{q}{kT} \frac{dV_{OC}}{d \ln \left(\frac{I}{I_0} \right)}, \quad (6)$$

where k is Boltzmann's constant, T is temperature, q is the elementary charge, $\frac{kT}{q}$ is the thermal voltage and is equal to 0.026 V at room temperature, and I_0 is reference intensity at one Sun.

Figure 7b displays the curves of V_{OC} changes against $\ln(I/I_0)$ and the slopes obtained for calculating the n_{id} values. The bulk and interfacial Shockley–Read–Hall (SRH) recombination are formulated according to Refs.^{58,59}.

$$R_{SRH} = \sigma_{n,p} \times N_t \times v_{th} \frac{np - n_i^2}{n + p + 2n_i \cosh \left(\frac{E_t - E_i}{kT} \right)}, \quad (7)$$

$$\tau_{n,p} = \frac{1}{\sigma_{n,p} \times N_t \times v_{th}}, \quad (8)$$

where n_i is the equilibrium charge density, $\sigma_{n,p}$ is the electron and hole absorption cross-section, and $n(p)$ is electron (hole) density under the non-equivalence condition. E_i and E_t represent the intrinsic and trap defect energy levels, respectively, v_{th} represents the thermal velocity and $\tau_{n,p}$ is the carrier lifetime. In Fig. 8, we can see the bulk and interfacial recombination currents, as well as cap V_{OC} s, and calculated n_{id} s. It's worth noting that band-to-band recombination was found to be negligible. In the PSC with bare ETL of MXene, the ideality factor is relatively close to 2 ($n_{id} = 1.60$).

When additive MXenes are introduced into the ETL of solar cells, the ideality factor values become closer to 1. This indicates that the interfacial mechanism, rather than bulk recombination, dominates in the MXene-assisted ETL cells. Among these cells, the one with 1.0 wt% of MXene shows the highest ideality factor and V_{OC} values. This suggests that adding 1.0 wt% of MXene into the SnO_2 ETL makes the interface recombination least effective, resulting in the best cell performance.

It is well established that incorporating MXenes in the structure of PSCs can enhance their performance. However, it is important to note that increasing the weight percentage of MXene in the SnO_2 ETL beyond 1.0 wt% may lead to a reduction in the V_{OC} , which requires further discussion. This same observation also applies to cells with 0.5 wt% of MXene. To remove ambiguities, we plotted the carrier lifetime of the absorber layer against the weight percentage of MXene in ETL (Fig. 9). It can be observed that the carrier lifetime reaches its peak when 1.0 wt% MXene is present in the SnO_2 ETL structure. This indicates that the charge carriers generated in this cell will have a longer effective time for extraction by the charge transport layers, in comparison to the other cells. In Fig. 10, the electric field distribution of cells at the ETL/absorber interface was studied for applied voltages that were less than, equal to, and greater than the V_{OC} . It was observed that the 1.0 wt% MXene-added cell had a stronger electric dipole formed at the ETL/absorber interface, which could establish a significant potential difference across the ETL. This would lead to a shorter extraction time for the electrons from the ETL, as compared to the charge carrier lifetime in the absorber layer^{34,60,61}. As a result, the photogenerated charge carriers in the absorber layer could be extracted immediately. On the other hand, due to the weaker dipole

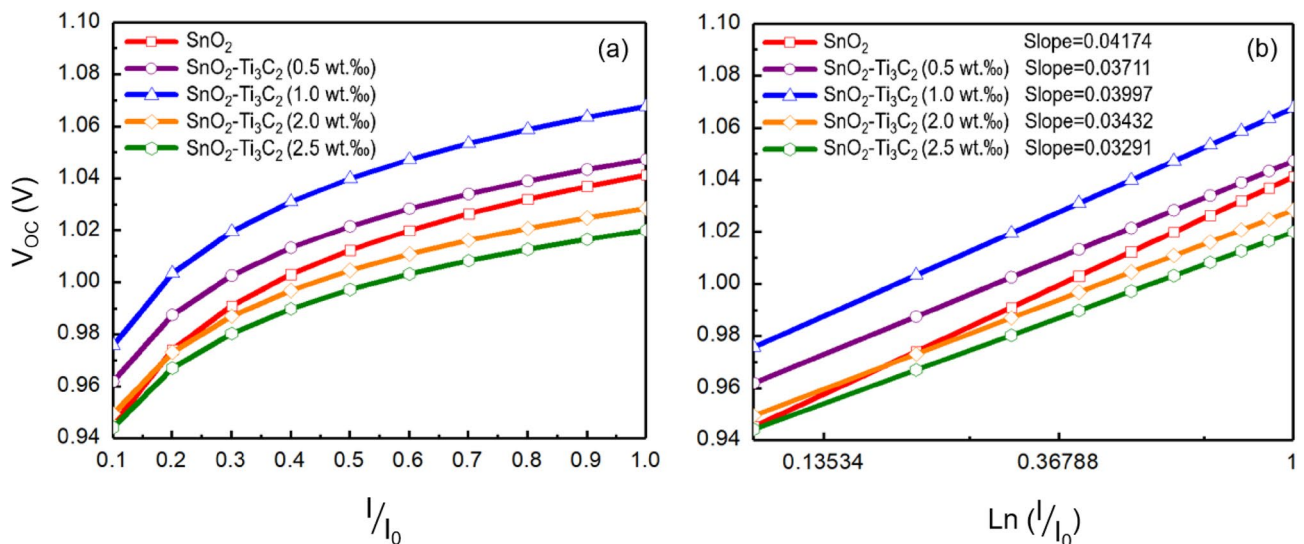


Figure 7. Plots of V_{OC} versus. (a) (I/I_0) , (b) the calculated slope of the V_{OC} versus $\ln(I/I_0)$ curves for PSCs with SnO_2 and MXene-assisted ETLs are shown.

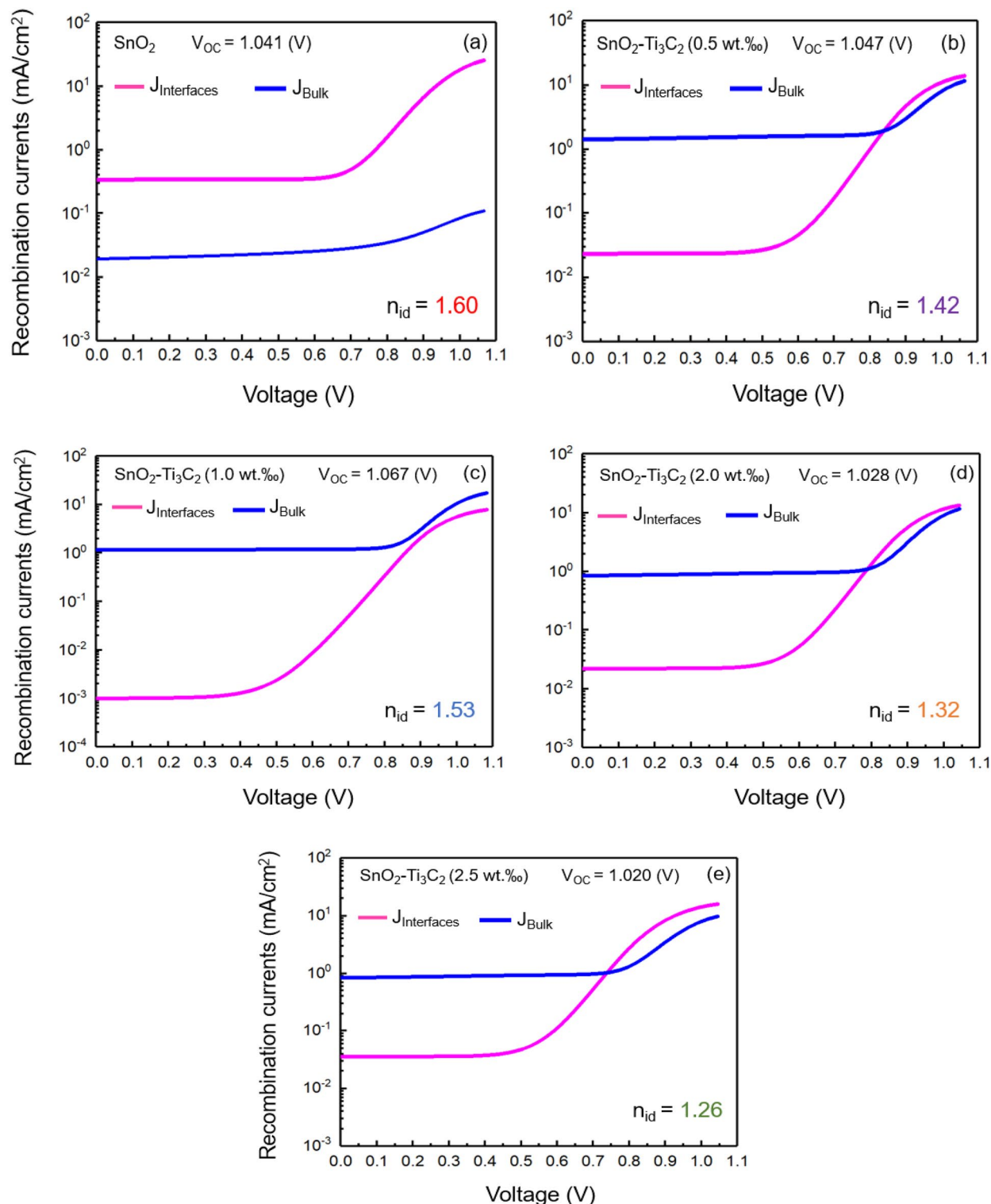


Figure 8. Bulk and interfacial recombination currents. The calculated open-circuit voltages and the ideality factors of each device are presented. (a) SnO₂, (b) SnO₂-Ti₃C₂ (0.5 wt.%), (c) SnO₂-Ti₃C₂ (1.0 wt.%), (d) SnO₂-Ti₃C₂ (2.0 wt.%), (e) SnO₂-Ti₃C₂ (2.5 wt.%).

moment of the other cells formed at the ETL/absorber, the photogenerated carriers took much more time to be collected. It has been observed that the addition of MXene to SnO₂ ETL cells results in higher recombination, which significantly reduces their overall performance. However, it has been found that the MXene-assisted cells with 1.0 wt% MXene-added-SnO₂ ETL show better performance compared to other such cells. This is due to the fact that interfacial recombination plays a more crucial role than bulk recombination in determining cell performance, as indicated by the higher ideality factor of these cells. In cells containing MXene, there is a

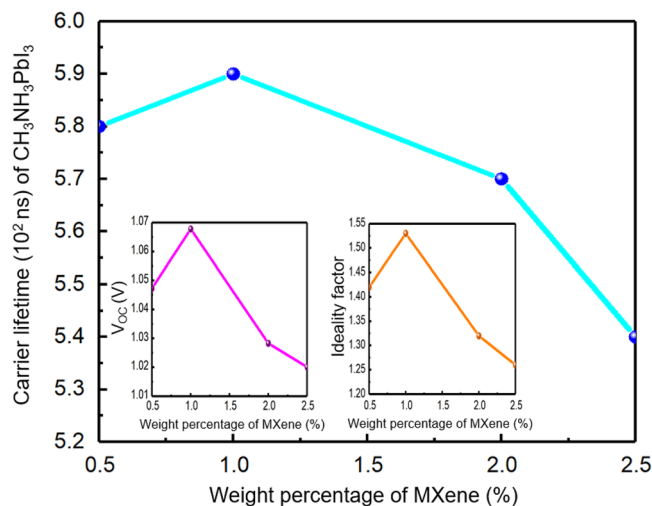


Figure 9. Carrier Lifetime of absorber layer curve vs MXene weight percentage (0.5, 1.0, 2.0, 2.5 wt%). Two insets depict the calculated V_{OC} and ideality factors varying with MXene weight percentage used in ETL.

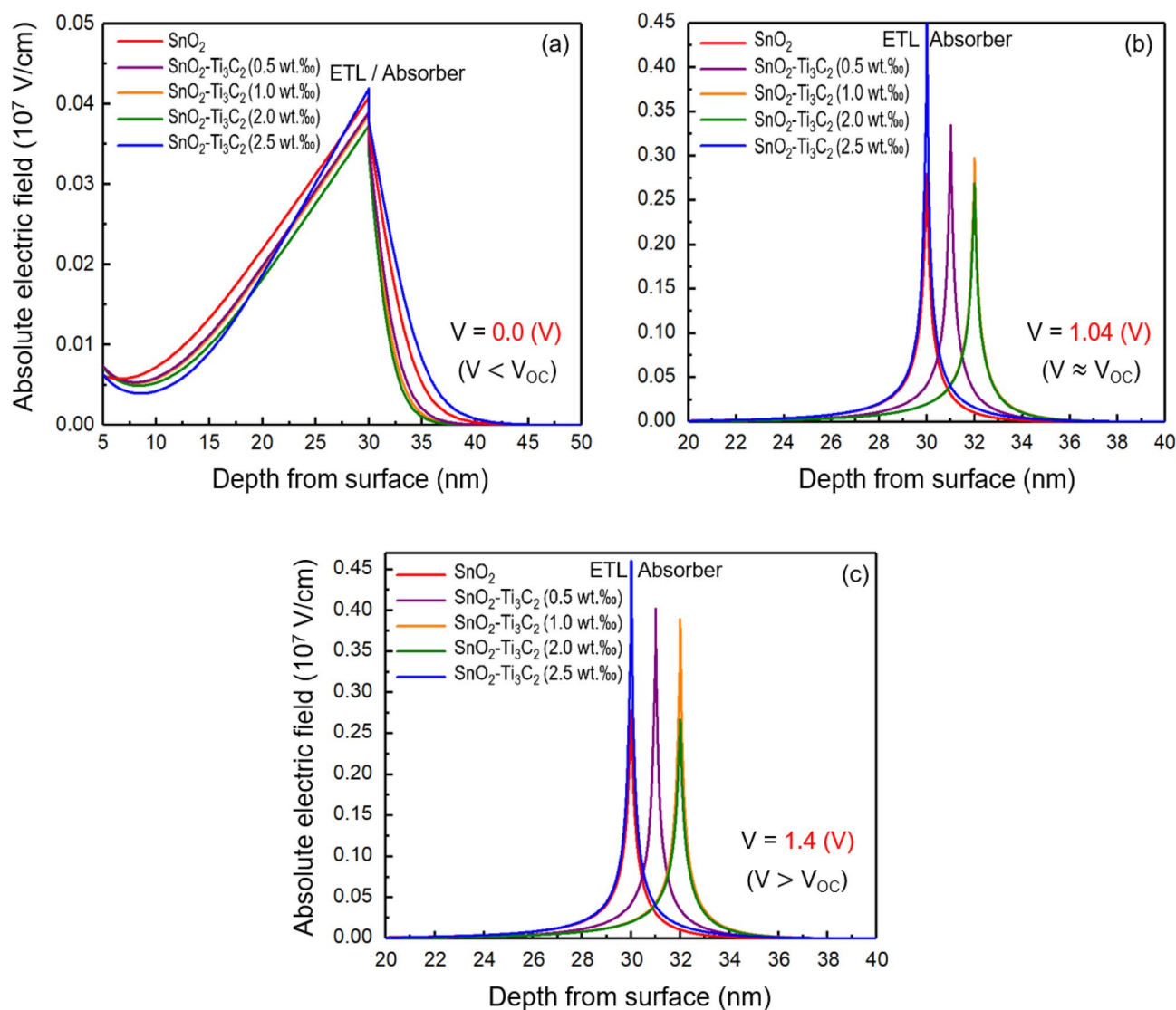


Figure 10. The Absolute electric field at the ETL/Absorber interface for $V < V_{OC}$ (a), $V \approx V_{OC}$ (b), and $V > V_{OC}$ (c).

correlation between n_{id} s and cell performance. This correlation can be explained through the inset in Fig. 9, where the curves of V_{OC} and n_{id} versus the MXene weight percentage follow the same pattern as the carrier lifetime in the absorber layer. Therefore, in these cells, a lower n_{id} indicates a higher interfacial recombination current, resulting in a less efficient cell.

In literature, the correlation between quasi-Fermi level splitting (QFLS) and charge carrier densities (n and p) in the absorber layer has been discussed (62).

$$QFLS = k_B T \ln \left(\frac{np}{n_i^2} \right) = k_B T \ln \left(\frac{n\beta}{n_i^2} \right) + const, \quad (9)$$

where β is a parameter defining the relationship between the carrier density and the perturbation of the QFLS from equilibrium and is equal to 1 or 2, and n_i is the equilibrium charge density. In brief, if the charge carrier densities undergo the condition $n \approx p$, the bulk recombination will dominate. Meanwhile, the presence of a dominant charge carrier, e.g., $n \gg p$ (or $p \gg n$), makes the interfacial recombination the dominant mechanism. Figure 11 shows n and p for cells with and without MXene, and Table 3 provides values of these values at the middle of the absorber layer. In the cell with bare SnO₂ ETL shows better $n \approx p$ is condition compared to the other cells. This indicated that bulk recombination dominates and n_{id} is likely to be close to 2. On the other hand, in MXene-assisted cells, the condition $n \gg p$ is satisfied, and the n_{id} is relatively close to 1. Among these cells, the one with 1.0 wt% of MXene has the lowest p/n ratio, which confirms the highest n_{id} .

After gaining more insights into the role of incorporated MXenes into the SnO₂ ETL, we assessed the photocurrent density using Eq. (10), where $J(V)$ and J_{dark} are the current density under light and the dark current density, respectively^{62,63}.

$$J_{ph} = J(V) - J_{dark}. \quad (10)$$

The electric field established in the absorber layer is $E = \frac{V_{bi}-V}{d}$, where V_{bi} is the built-in potential, and d is the thickness⁶¹. The drift caused by such an internal electric field makes a photogenerated current. This photogenerated current $J_{ph}(V)$ is formulated as^{64,65},

$$\begin{aligned} J_{ph}(V) &= |J_{sc}| \text{if } \mu\tau \frac{V_{bi}-V}{d} > d, \\ J_{ph}(V) &= -|J_{sc}| \text{if } \mu\tau \frac{V-V_{bi}}{d} > d, \\ J_{ph}(V) &= |J_{sc}| \frac{\mu\tau(V_{bi}-V)}{d^2} \text{ else,} \end{aligned} \quad (11)$$

where μ is charge carrier mobility, τ is charge carrier lifetime, V is the applied voltage, and d is the sample thickness. The equation above provides a practical method to determine the built-in potential by finding the intersection of the $J_{ph}(V)$ curve with the voltage axis.

Figure 12 illustrates the $J_{ph}(V)$ of the cells with and without MXene in their ETL structure. This figure clarifies how to derive the V_{bi} for each sample. Improving the V_{OC} is crucial in photovoltaic structures as it effectively reduces interfacial recombination. On the other hand, the voltage limit of the V_{OC} is determined by the V_{bi} which is vital for achieving better cell performance⁶⁶⁻⁷⁰. As depicted in the figure, the sample containing 1.0 wt.% MXene in the ETL displays the highest V_{bi} , which is why it has the highest PCE among all samples.

In the last part of this work, an optimization procedure of the SnO₂-Ti₃C₂ (1.0 wt%) is presented, and it is hoped that the results of this optimization will have a significant impact on practical features of photovoltaic science, as well as understanding the role of the thickness of the layers.

Figure 13 shows a contour plot that displays the variation of the thickness of the SnO₂-Ti₃C₂ (1.0 wt%) ETL and the absorber layer, ranging from 10 to 40 nm and 400 nm to 1200 nm, respectively. The optimal thickness for the absorber layer is 700 nm, while the optimal thickness for the ETL is 10 nm. We will use these values for the ETL and absorber thickness parameters throughout the optimization process.

Figure 14 illustrates the relationship between the thickness of the HTL and the absorber. The range of HTL layer thickness considered in this study is between 100 and 700 nm. After optimization, a thickness of 700 nm was selected as the most suitable for the HTL layer thickness.

Figure 15 displays the J-V and power density-voltage (P-V) curves, which were plotted based on the optimized parameters discussed earlier for the MXene-assisted cell with SnO₂-Ti₃C₂ (1.0 wt%) ETL. The photovoltaic response of the optimized MXene-assisted cell with SnO₂-Ti₃C₂ (1.0 wt%) ETL was achieved through $J_{SC} = 36.21$ mA/cm², $V_{OC} = 1.051$ (V), FF = 73.07% and PCE = 27.81%, respectively.

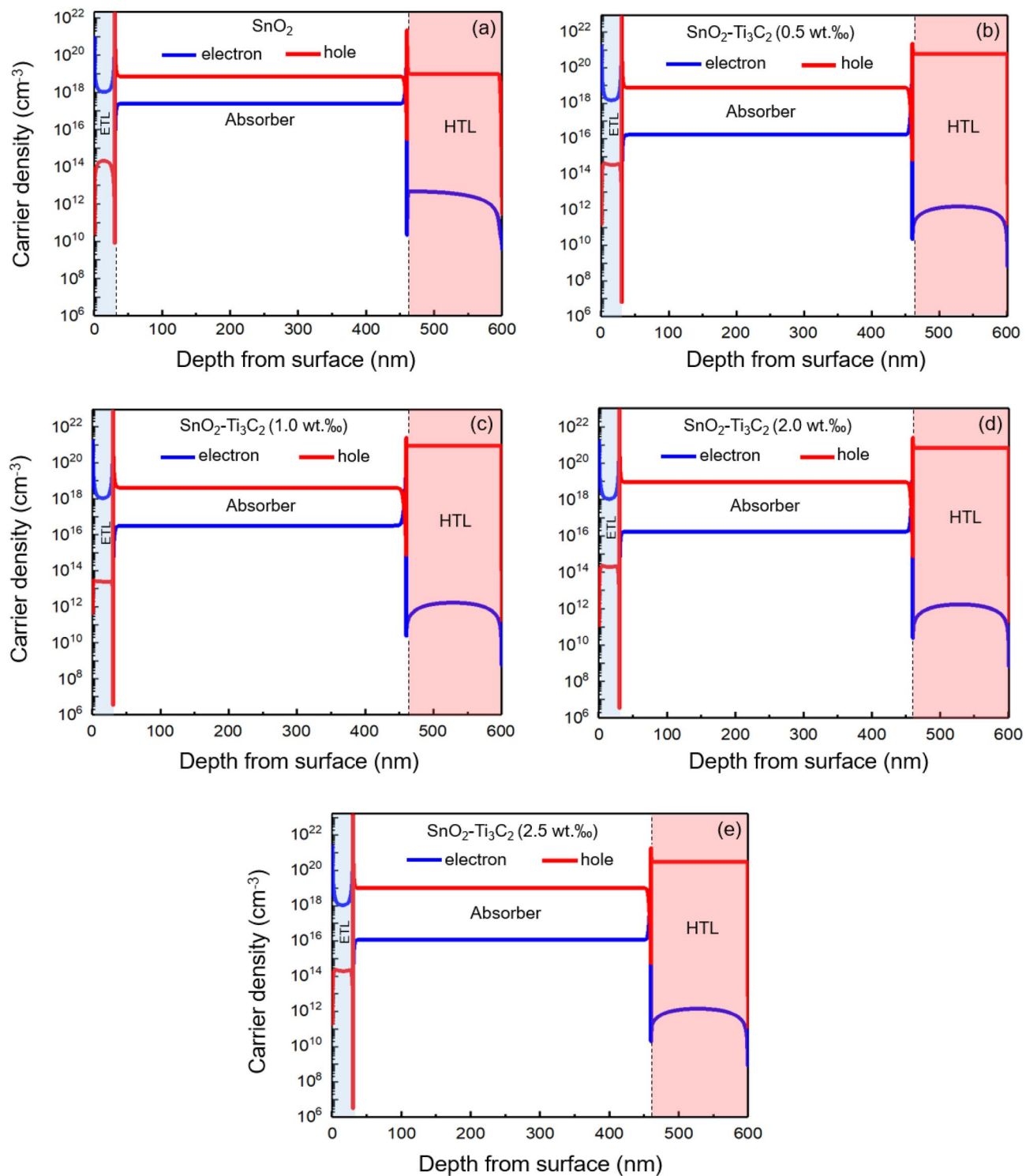


Figure 11. Charge carrier density across the absorber and charge transport layers of the cells with and without MXene. (a) SnO_2 , (b) $\text{SnO}_2\text{-Ti}_3\text{C}_2$ (0.5 wt.%), (c) $\text{SnO}_2\text{-Ti}_3\text{C}_2$ (1.0 wt.%), (d) $\text{SnO}_2\text{-Ti}_3\text{C}_2$ (2.0 wt.%), (e) $\text{SnO}_2\text{-Ti}_3\text{C}_2$ (2.5 wt.%).

ETLs	p	n	p/n
SnO ₂	7.2×10^{18}	2.4×10^{17}	3.0×10^1
SnO ₂ -Ti ₃ C ₂ (0.5 wt%)	7.6×10^{18}	1.7×10^{16}	4.5×10^2
SnO ₂ -Ti ₃ C ₂ (1.0 wt%)	4.0×10^{18}	3.1×10^{16}	1.3×10^2
SnO ₂ -Ti ₃ C ₂ (2.0 wt%)	9.0×10^{18}	1.7×10^{16}	5.3×10^2
SnO ₂ -Ti ₃ C ₂ (2.5 wt%)	1.0×10^{19}	1.2×10^{16}	8.3×10^2

Table 3. Electron (hole) density values in the PSCs.

Conclusion

A numerical analysis was conducted on devices with and without 2D MXene in their SnO₂ ETLs using SCAPS-1D software. The study found that a device architecture of ITO/ETL/CH₃NH₃PbI₃/Spiro-OMeTAD/Ag with SnO₂-Ti₃C₂ (1.0 wt%) as the ETL achieved a relatively high PCE of 27.81%. It is believed that the added MXene plays a crucial role in reducing the interfacial recombination, which is the primary reason for the improved performance of the cell. By calculating the ideality factor (n_{id}), we established a correlation between this quantity and the cell performance. We found that the sample with the highest efficiency also had the highest n_{id} value of 1.53. The improvement in efficiency in PSCs can be credited to the increase in R_{rec} , a parameter that explains the enhancement in efficiency. This parameter demonstrates that IS is an easy and alternative technique for obtaining information about PSCs.

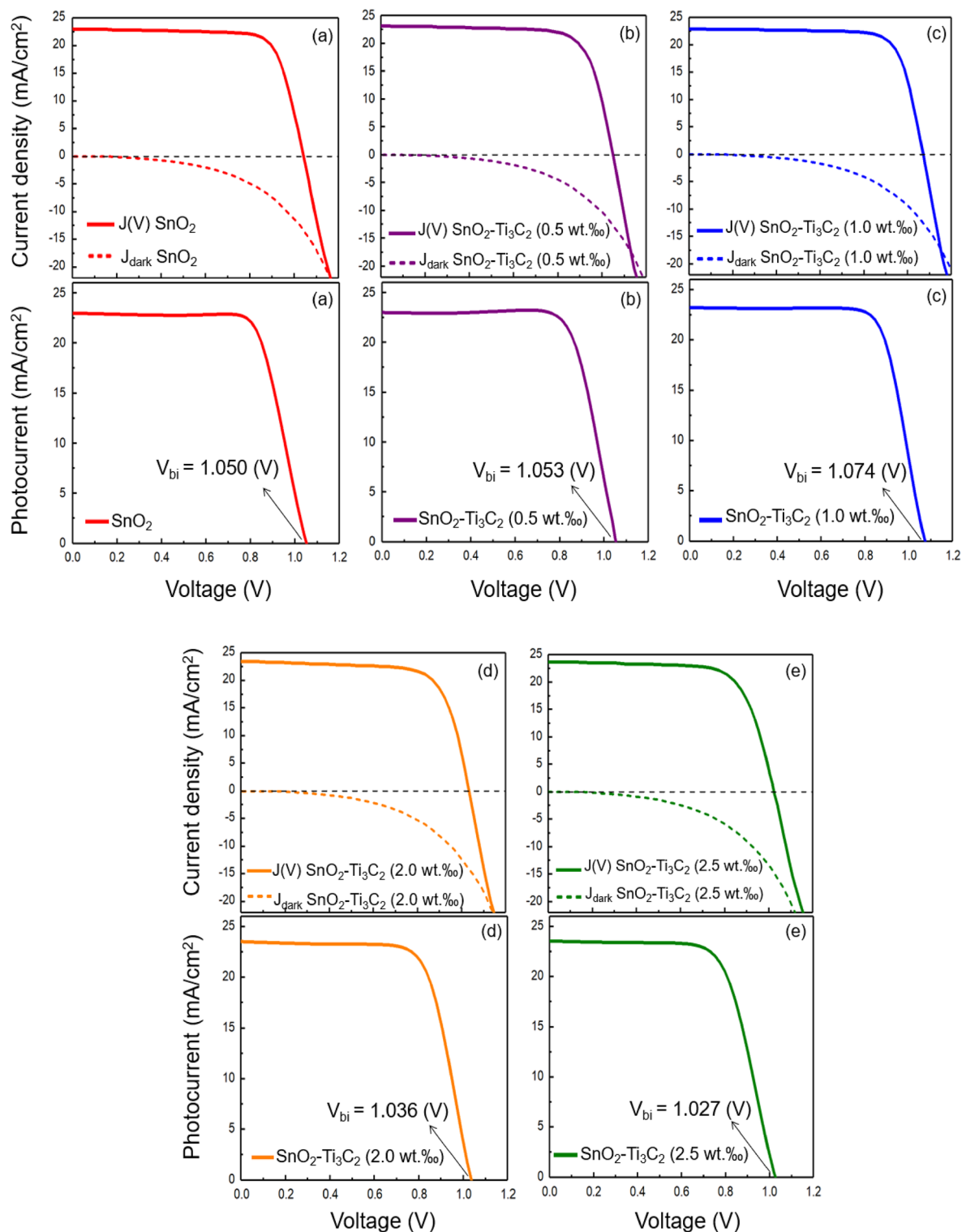


Figure 12. The current and photocurrent densities of PSCs with different ETLs. (a) SnO_2 , (b) $\text{SnO}_2\text{-Ti}_3\text{C}_2$ (0.5 wt.%), (c) $\text{SnO}_2\text{-Ti}_3\text{C}_2$ (1.0 wt.%), (d) $\text{SnO}_2\text{-Ti}_3\text{C}_2$ (2.0 wt.%), (e) $\text{SnO}_2\text{-Ti}_3\text{C}_2$ (2.5 wt.%).

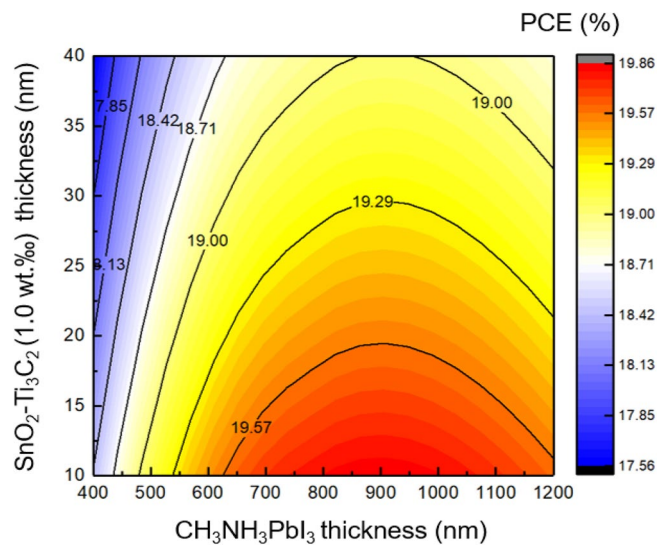


Figure 13. The effect of the $\text{SnO}_2\text{-Ti}_3\text{C}_2$ (1.0 wt.%) ETL and absorber thickness variation on the cell performance.

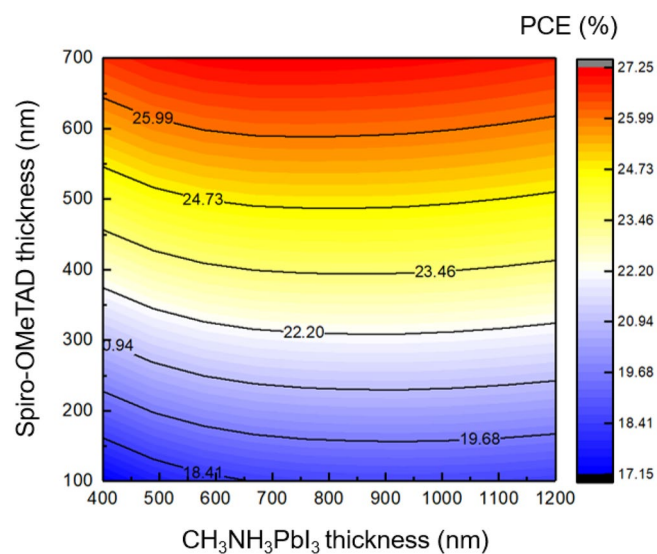


Figure 14. The effect of the HTL and absorber thickness variation on the cell performance.

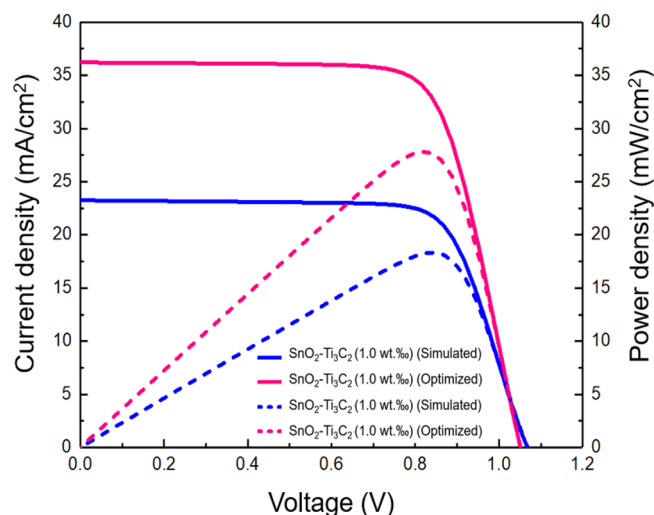


Figure 15. J–V (solid lines) and P–V (dashed lines) for the MXene-assisted cell with SnO₂–Ti₃C₂ (1.0 wt%) ETL.

Data availability

The datasets generated during and/or analysed during the current study are available from the corresponding author on reasonable request.

Received: 15 November 2023; Accepted: 6 March 2024

Published online: 08 March 2024

References

- Kojima, A., Teshima, K., Shirai, Y. & Miyasaka, T. Organometal halide perovskites as visible-light sensitizers for photovoltaic cells. *J. Am. Chem. Soc.* **131**, 6050–6051. <https://doi.org/10.1021/ja809598r> (2009).
- Chandel, R., Punetha, D., Dhawan, D. & Gupta, N. Optimization of highly efficient and eco-friendly EA-substituted tin-based perovskite solar cell with different hole transport material. *Opt. Quant. Electron.* **54**(6), 337. <https://doi.org/10.1007/s11082-022-03740-6> (2022).
- Burschka, J. *et al.* Sequential deposition as a route to high-performance perovskite-sensitized solar cells. *Nature* **499**, 316–319. <https://doi.org/10.1038/nature12340> (2013).
- Bhattacharai, S. & Das, T. D. Optimization of carrier transport materials for the performance enhancement of the MAgE₃-based perovskite solar cell. *Solar Energy* **217**, 200–207. <https://doi.org/10.1016/j.solener.2021.02.002> (2021).
- Yin, W. J., Shi, T. & Yan, Y. Unique properties of halide perovskites as possible origins of the superior solar cell performance. *Adv. Mater.* **26**, 4653–4658. <https://doi.org/10.1002/adma.201306281> (2014).
- Stranks, S. D. *et al.* Electron–hole diffusion lengths exceeding 1 micrometer in an organometal trihalide perovskite absorber. *Science* **342**, 341–344. <https://doi.org/10.1126/science.1243982> (2013).
- Li, Y. *et al.* High-efficiency robust perovskite solar cells on ultrathin flexible substrates. *Nat. Commun.* **7**, 10214. <https://doi.org/10.1038/ncomms10214> (2016).
- Bhattacharai, S. *et al.* Carrier transport layer free perovskite solar cell for enhancing the efficiency: A simulation study. *Optik Int. J. Light Electron Opt.* **243**, 167492. <https://doi.org/10.1016/j.ijleo.2021.167492> (2021).
- Bhattacharai, S. *et al.* Optimized high-efficiency solar cells with dual hybrid halide perovskite absorber layers. *Energy Fuels* **37**, 16022–16034. <https://doi.org/10.1021/acs.energyfuels.3c02099> (2023).
- Bhattacharai, S. *et al.* Performance improvement of hybrid-perovskite solar cells with double active layer design using extensive simulation. *Energy Fuels* **37**(21), 16893–16903. <https://doi.org/10.1021/acs.energyfuels.3c02478> (2023).
- Bhattacharai, S., Pandey, R., Madan, J., Ahmed, F. & Shabnam, S. Performance improvement approach of all inorganic perovskite solar cell with numerical simulation. *Mater. Today Commun.* **33**(17), 104364. <https://doi.org/10.1016/j.mtcomm.2022.104364> (2022).
- Ke, W. *et al.* Low-temperature solution-processed tin oxide as an alternative electron transporting layer for efficient perovskite solar cells. *J. Am. Chem. Soc.* **137**, 6730–6733. <https://doi.org/10.1021/jacs.5b01994> (2015).
- Yang, G. *et al.* Effective carrier-concentration tuning of SnO₂ quantum dot electron-selective layers for high-performance planar perovskite solar cells. *Adv. Mater.* **30**(14), 1706023. <https://doi.org/10.1002/adma.201706023> (2018).
- Song, J. *et al.* Low-temperature SnO₂-based electron selective contact for efficient and stable perovskite solar cells. *J. Mater. Chem. A* **3**, 10837–10844. <https://doi.org/10.1039/c5ta01207d> (2015).
- Patel, P. K. Device simulation of highly efficient eco-friendly CH₃NH₃SnI₃ perovskite solar cell. *Sci. Rep.* **11**, 3082. <https://doi.org/10.1038/s41598-021-82817-w> (2021).
- Dong, Q., Shi, Y., Zhang, C., Wu, Y. & Wang, L. Energetically favored the formation of SnO₂ nanocrystals as electron transfer layer in perovskite solar cells with high efficiency exceeding 19%. *Nano Energy* **40**, 336–344. <https://doi.org/10.1016/j.nanoen.2017.08.041> (2017).
- Anaraki, E. H. *et al.* Highly efficient and stable planar perovskite solar cells by solution-processed tin oxide. *Energy Environ. Sci.* **9**, 3128–3134. <https://doi.org/10.1039/C6EE02390H> (2016).
- Zakaria, Y. *et al.* Moderate temperature deposition of RF magnetron sputtered SnO₂-based electron transporting layer for triple cation perovskite solar cells. *Sci. Rep.* **13**, 9100. <https://doi.org/10.1038/s41598-023-35651-1> (2023).
- Guo, H. *et al.* TiO₂/SnO₂ nanocomposites as electron transporting layer for efficiency enhancement in planar CH₃NH₃PbI₃-based perovskite solar cells. *ACS Appl. Energy Mater.* **1**(12), 6936–6944. <https://doi.org/10.1021/acs.aem.8b01331> (2018).

20. Park, M. *et al.* Low-temperature solution-processed Li-doped SnO₂ as an effective electron transporting layer for high-performance flexible and wearable perovskite solar cells. *Nano Energy* **26**, 208–215. <https://doi.org/10.1016/j.nanoen.2016.04.060> (2016).
21. Yang, G. *et al.* Reducing hysteresis and enhancing performance of perovskite solar cells using low-temperature processed Y-doped SnO₂ nanosheets as electron selective layers. *Small* **13**, 1601769. <https://doi.org/10.1002/smll.201601769> (2016).
22. Yun, T. *et al.* Electromagnetic shielding of monolayer MXene assemblies. *Adv. Mater.* **32**(9), 1906769. <https://doi.org/10.1002/adma.201906769> (2020).
23. Hantanasirisakul, K. & Gogotsi, Y. Electronic and optical properties of 2D transition metal carbides and nitrides (MXenes). *Adv. Mater.* **30**, 1804779. <https://doi.org/10.1002/adma.201804779> (2018).
24. Ahmad, Z. *et al.* Consequence of aging at Au/HTM/perovskite interface in triple cation 3D and 2D/3D hybrid perovskite solar cells. *Sci. Rep.* **11**, 33. <https://doi.org/10.1038/s41598-020-79659-3> (2021).
25. Naguib, M. *et al.* Two-dimensional nanocrystals produced by exfoliation of Ti₃AlC₂. *Adv. Mater.* **23**, 4248–4253. <https://doi.org/10.1002/adma.201102306> (2011).
26. Agresti, A. *et al.* Two-dimensional material interface engineering for efficient perovskite large-area modules. *ACS Energy Lett.* **4**(8), 1862–1871. <https://doi.org/10.1021/acsenergylett.9b01151> (2019).
27. Khazaei, M., Ranjbar, A., Arai, M., Sasaki, T. & Yunoki, S. Electronic properties and applications of MXenes: A theoretical review. *J. Mater. Chem. C* **5**, 2488–2503. <https://doi.org/10.1039/C7TC00140A> (2017).
28. Agresti, A. *et al.* Titanium carbide MXenes for a work function and interface engineering in perovskite solar cells. *Nat. Mater.* **18**, 1228–1234. <https://doi.org/10.1038/s41563-019-0478-1> (2019).
29. Guo, J. *et al.* Cold sintered ceramic nanocomposites of 2D MXene and zinc oxide. *Adv. Mater.* **30**(32), 1801846. <https://doi.org/10.1002/adma.201801846> (2018).
30. Kakavelakis, G., Kymakis, E. & Petridis, K. Interfaces, 2D materials beyond graphene for metal halide perovskite solar cells. *Adv. Mater.* **5**, 1800339. <https://doi.org/10.1002/admi.201800339> (2018).
31. Caprioglio, P. *et al.* On the origin of the ideality factor in perovskite solar cells. *Adv. Energy Mater.* **10**, 2000502. <https://doi.org/10.1002/aenm.202000502> (2020).
32. Liu, Y., Xiao, H. & Goddard, W. A. Schottky-barrier-free contacts with two-dimensional semiconductors by surface-engineered MXenes. *J. Am. Chem. Soc.* **138**(49), 15853–15856. <https://doi.org/10.1021/jacs.6b10834> (2016).
33. Wang, Y. *et al.* MXene-modulated electrode/SnO₂ interface boosting charge transport in perovskite solar cells. *ACS Appl. Mater. Interfaces* **12**(48), 53973–53983. <https://doi.org/10.1021/acsami.0c17338> (2020).
34. Yang, L. *et al.* SnO₂-Ti₃C₂ MXene electron transport layers for perovskite solar cells. *J. Mater. Chem. A* **7**, 5635–5642. <https://doi.org/10.1039/c8ta12140k> (2019).
35. Xu, Y. *et al.* MXene regulates the stress of perovskite and improves interface contact for high-efficiency carbon-based all-inorganic solar cells. *Chem. Eng. J.* **461**, 141895. <https://doi.org/10.1016/j.cej.2023.141895> (2023).
36. Akuzum, B. *et al.* Rheological characteristics of 2D titanium carbide (MXene) dispersions: A guide for processing MXenes. *ACS Nano* **12**(3), 2685–2694. <https://doi.org/10.1021/acsnano.7b08889> (2018).
37. Caprioglio, P., Wolff, C. M., Neher, D. & Stollerfoht, M. On the Origin of ideality factor in perovskite solar cells. *Adv. Energy Mater.* **10**, 2000502. <https://doi.org/10.1002/aenm.202000502> (2020).
38. Almora, O. *et al.* Discerning recombination mechanisms and ideality factors through impedance analysis of high-efficiency perovskite solar cells. *Nano Energy* **48**, 63–72. <https://doi.org/10.1016/j.nanoen.2018.03.042> (2018).
39. Maklavani, S. E. & Mohammadnejad, S. The impact of the carrier concentration and recombination current on the p+pn CZTS thin film solar cells. *Opt. Quant. Electron.* **52**(6), 279. <https://doi.org/10.1007/s11082-020-02407-4> (2020).
40. Lvovich, V. F. *Impedance Spectroscopy: Applications to Electrochemical and Dielectric Phenomena* (Wiley, 2012).
41. Adhitya, K., Alsulami, A., Buckley, A., Tozer, R. C. & Grell, M. Intensity-modulated spectroscopy on loaded organic photovoltaic cells. *IEEE J. Photovolt.* **5**(5), 1414–1421. <https://doi.org/10.1109/JPHOTOV.2015.2447838> (2015).
42. Yi, H. *et al.* Bilayer SnO₂ as an electron transport layer for highly efficient perovskite solar cells. *ACS Appl. Energy Mater.* **1**, 6027–6039. <https://doi.org/10.1021/acsaem.8b01076> (2018).
43. von Hauff, E. & Klotz, D. Impedance spectroscopy for perovskite solar cells: Characterization, analysis, and diagnosis. *J. Mater. Chem. C* **10**, 742–761. <https://doi.org/10.1039/D1TC04727B> (2022).
44. Anasori, B. *et al.* Two-dimensional, ordered, double transition metals carbides (MXenes). *ACS Nano* **9**, 9507–9516. <https://doi.org/10.1021/acsnano.5b03591> (2015).
45. Decock, K., Zabierowski, P. & Burgelman, M. Modeling metastabilities in chalco-pyrite-based thin film solar cells. *J. Appl. Phys.* **111**, 043703. <https://doi.org/10.1063/1.3686651> (2012).
46. Mohandes, A., Nadgaran, H. & Manadi, M. Numerical simulation of inorganic Cs₂AgBiBr₆ as a lead-free perovskite using device simulation SCAPS-1D. *Opt. Quant. Electron.* **53**(6), 319. <https://doi.org/10.1007/s11082-021-02959-z> (2021).
47. Rahman, A. Design and simulation of a high-performance Cd-free Cu₂SnSe₃ solar cells with SnS electron-blocking hole transport layer and TiO₂ electron transport layer by SCAPS-1D. *SN Appl. Sci.* **3**(2), 253. <https://doi.org/10.1007/s42452-021-04267-3> (2021).
48. Luszczyk, G., Swisulski, D. & Luszczyk, M. Simulation investigation of perovskite-based solar cells. *Przeegląd Elektrotech.* **97**(5), 99–102. <https://doi.org/10.15199/48.2021.05.17> (2021).
49. Asgharizadeh, S. & Azadi, S. K. *The Device Simulation of MXene-added Hole-Transport Free Perovskite Solar Cells*. LicenseCC BY 4.0. <https://doi.org/10.21203/rs.3.rs-2250561/v1> (2022).
50. Otofui, M. K. Enhanced performance of planer perovskite solar cell using TiO₂/SnO₂ and TiO₂/WO₃ bilayer structures: Roles of the interfacial layers. *Solar Energy* **208**, 697–707. <https://doi.org/10.1016/j.solener.2020.08.035> (2020).
51. Huo, Y., Liou, P., Li, Y., Sun, L. & Kloo, L. Composite hole-transport materials based on a metal–organic copper complex and spiro-OMeTAD for efficient perovskite solar cells. *Solar RRL* **2**(5), 1700073. <https://doi.org/10.1002/solr.201700073> (2018).
52. Rajesh, K. & Santhanalakshmi, J. Fabrication of a SnO₂-graphene nanocomposite-based electrode for sensitive monitoring of an anti-tuberculosis agent in human fluids. *N. J. Chem.* **42**, 2903–2915. <https://doi.org/10.1039/C7NJ03411C> (2018).
53. Saliba, M. & Etgar, L. Current density mismatch in perovskite solar cells. *ACS Energy Lett.* **5**, 2886–2888. <https://doi.org/10.1021/acsenergylett.0c01642> (2020).
54. Hens, Z. & Gomes, W. P. Electrochemical impedance spectroscopy at semiconductor electrodes: The recombination resistance revisited. *J. Electroanal. Chem.* **437**, 77–83. [https://doi.org/10.1016/S0022-0728\(97\)00092-2](https://doi.org/10.1016/S0022-0728(97)00092-2) (1997).
55. van den Meerakker, J. E. A. M., Kelly, J. J. & Notten, P. H. L. The minority carrier recombination resistance: A useful concept in semiconductor electrochemistry. *J. Electrochem. Soc.* **132**, 638–642. <https://doi.org/10.1149/1.2113920> (1985).
56. Khorasani, A. E., Schroder, D. K. & Alford, T. L. Optically excited MOS-capacitor for recombination lifetime measurement. *IEEE Electron. Device Lett.* **35**(10), 986–988. <https://doi.org/10.1109/LED.2014.2345058> (2014).
57. Calado, P. *et al.* Identifying dominant recombination mechanisms in perovskite solar cells by measuring the transient ideality factor. *Phys. Rev. Appl.* **11**, 044005. <https://doi.org/10.1103/PhysRevApplied.11.044005> (2019).
58. Ryu, S., Ha, N. Y., Ahn, Y. H., Park, J.-Y. & Lee, S. Light intensity dependence of organic solar cell operation and dominance switching between Shockley–Read–Hall and bimolecular recombination losses. *Sci. Rep.* **11**, 16781. <https://doi.org/10.1038/s41598-021-96222-w> (2021).
59. Nazerdeylami, S. & Dizaji, H. R. Influence of exponential tail states on photovoltaic parameters and recombination of bulk heterojunctionorganic solar cells: An optoelectronic simulation. *Opt. Quant. Electron.* **48**(4), 260. <https://doi.org/10.1007/s11082-016-0541-y> (2016).

60. Asgharizadeh, S. & Azadi, S. K. Additive MXene and dominant recombination channel in perovskite solar cells. *Solar Energy* **241**, 720–727. <https://doi.org/10.1016/j.solener.2022.07.001> (2022).
61. Asgharizadeh, S., Azadi, S. K. & Lazemi, M. Understanding the pathways toward improved efficiency in MXene-assisted perovskite solar cells. *J. Mater. Chem. C* **10**, 1776–1786. <https://doi.org/10.1039/D1TC04643H> (2022).
62. Wehenkel, D. J., Koster, L. J. A., Wienk, M. M. & Janssen, R. A. J. Influence of injected charge carriers on photocurrents in polymer solar cells. *Phys. Rev. B* **85**, 125203. <https://doi.org/10.1103/PhysRevB.85.125203> (2012).
63. Petersen, A., Kirchartz, T. & Wagner, T. A. Charge extraction and photocurrent in organic bulk heterojunction solar cells. *Phys. Rev. B* **85**, 045208. <https://doi.org/10.1103/physrevb.85.045208> (2012).
64. Tress, W., Leo, K. & Riede, M. Optimum mobility, contact properties, and open-circuit voltage of organic solar cells: A drift-diffusion simulation study. *Phys. Rev. B* **85**, 155201. <https://doi.org/10.1103/PhysRevB.85.155201> (2012).
65. Sandberg, O. J., Sundqvist, A., Nyman, M. & Sandberg, R. O. Relating charge transport, contact properties, and recombination to open-circuit voltage in sandwich-type thin-film solar cells. *Phys. Rev. Appl.* **5**, 044005. <https://doi.org/10.1103/PhysRevApplied.5.044005> (2016).
66. Tessler, N. & Vaynzof, Y. Insights from device modeling of perovskite solar cells. *ACS Energy Lett.* **5**(4), 1260–1270. <https://doi.org/10.1021/acsenergylett.0c00172> (2020).
67. Cai, L., Wang, Y., Ning, L. & Syed, A. A. Effect of precursor aging on built-in potential in formamidinium-based perovskite solar cells. *Energy Technol.* **8**(12), 2000192. <https://doi.org/10.1002/ente.202000192> (2020).
68. Mingeback, M. & Deibe, C. Built-in potential and validity of Mott–Schottky analysis in organic bulk heterojunction solar cells. *Phys. Rev. B* **84**, 153201. <https://doi.org/10.1103/PhysRevB.84.153201> (2011).
69. Kirchartz, T. High open-circuit voltages in lead-halide perovskite solar cells: Experiment, theory and open questions. *Philos. Trans. R. Soc. A* **377**, 20180286. <https://doi.org/10.1098/rsta.2018.0286> (2019).
70. Sinha, N. K., Ghosh, D. S. & Khare, A. Role of built-in potential over ETL/perovskite interface on the performance of HTL-free perovskite solar cells. *Opt. Mater.* **129**, 112517. <https://doi.org/10.1016/j.optmat.2022.112517> (2022).

Author contributions

All authors contributed to the study conception and design. Material preparation, data collection, and analysis were performed by Mahdiyeh Meskini and Saeid Asgharizadeh. The first draft of the manuscript was written by Mahdiyeh Meskini and all authors commented on previous versions of the manuscript. All authors read and approved the final manuscript.

Competing interests

The authors declare no competing interests.

Additional information

Correspondence and requests for materials should be addressed to M.M.

Reprints and permissions information is available at www.nature.com/reprints.

Publisher's note Springer Nature remains neutral with regard to jurisdictional claims in published maps and institutional affiliations.



Open Access This article is licensed under a Creative Commons Attribution 4.0 International License, which permits use, sharing, adaptation, distribution and reproduction in any medium or format, as long as you give appropriate credit to the original author(s) and the source, provide a link to the Creative Commons licence, and indicate if changes were made. The images or other third party material in this article are included in the article's Creative Commons licence, unless indicated otherwise in a credit line to the material. If material is not included in the article's Creative Commons licence and your intended use is not permitted by statutory regulation or exceeds the permitted use, you will need to obtain permission directly from the copyright holder. To view a copy of this licence, visit <http://creativecommons.org/licenses/by/4.0/>.

© The Author(s) 2024